Int J Adv Manuf Technol (2016) 86:2621–2633
DOI 10.1007/s00170-016-8360-7

ORIGINAL ARTICLE

Constitutive relationship of 4Cr9Si2 and technological parameters on the inner bore of cross wedge rolling for preform hollow valves

Hongchao Ji[1] · Jinping Liu[1] · Baoyu Wang[1] · Xuefeng Tang[1] · Yuanming Huo[1] · Jing Zhou[1] · Zhenghuan Hu[1]

Received: 15 October 2015 / Accepted: 13 January 2016 / Published online: 29 January 2016

Abstract The hot deformation behavior of 4Cr9Si2 heat-resistant steel was investigated by hot deformation compression tests in the deformation temperature range of 950–1180 °C with strain rates of 0.1–10 s^{-1}. The constitutive equation of 4Cr9Si2 heat-resistant steel was established to describe the peak stress as a function of the deformation temperature and strain rate. The deformation characteristics of the cross wedge rolling (CWR) process of preform hollow valves are analyzed. By using DEFORM-3D software for finite element simulation tools, the process of CWR forming hollow valves was analyzed. According to the finite element simulation results, which reveal the influence of different process parameters on the inner diameter of the hollow valve blank, changing the stretching angle of the die design method effectively improves the position wedge reaming of the workpiece.

Keywords Constitutive equation · 4Cr9Si2 · Cross wedge rolling · Hollow valves · Inner bore

1 Introduction

A hollow valve is a special form of valve, and the heat-resistant alloy material of the inlet valve is 40Cr and 4Cr9Si2. The heat-resistant alloy material of the exhaust valve is 21-2N, 21-4N, and 4Cr10Si2Mo [1–4]. Thus, the weight of the hollow valves can be decreased significantly. Moreover, the hollow part of a closed cycle can cool the liquid sodium, decrease the working temperature, save energy, and reduce emissions. Hollow valves are more efficient than solid valves. Therefore, hollow valves must be produced for new-generation vehicles. Two methods are used to produce hollow valves: drilling into solid valves and reverse extrusion [5]. However, these methods have many disadvantages: (1) high manufacturing costs, (2) low production efficiency, (3) low material utilization ratio, and (4) complex manufacturing process. Given the current mode of production, the requirements of modern manufacturing are difficult to meet. Therefore, an advanced manufacturing technology must be developed for hollow valve production.

CWR is a plastic forming process wherein cylindrical workpieces are deformed into axisymmetric-stepped parts by using two or more wedge tools that move along the tangent direction of these workpieces [6–10]. The process is performed at an elevated temperature to generate low deformation forces. CWR possesses the following advantages: high production efficiency, low material cost, and high material utilization rate. Scholars have conducted many studies on CWR solid pieces [11–14]. Pater [11] analyzed the CWR process by theoretical and experimental methods. Lovell et al. [12, 13] presented an analytical method to evaluate the friction condition that prevents the slipping of a workpiece between tools. Xiong et al. [14] studied the effect of warm CWR on microstructure and mechanical property of high-carbon steel rods.

A number of studies have been conducted on the CWR process for hollow shaft production [15–26]. Lovell et al. [15, 16] studied CWR theory and technology for hollow shaft parts. Experiments and FE simulations were performed to determine the unstable conditions induced when the hollow shaft

✉ Jinping Liu
jhustb13@gmail.com; liujp@ustb.edu.cn

✉ Baoyu Wang
bywang@ustb.edu.cn

[1] School of Mechanical Engineering, University of Science and Technology Beijing, No. 30 Xueyuan Road, Haidian District, Beijing 100083, China

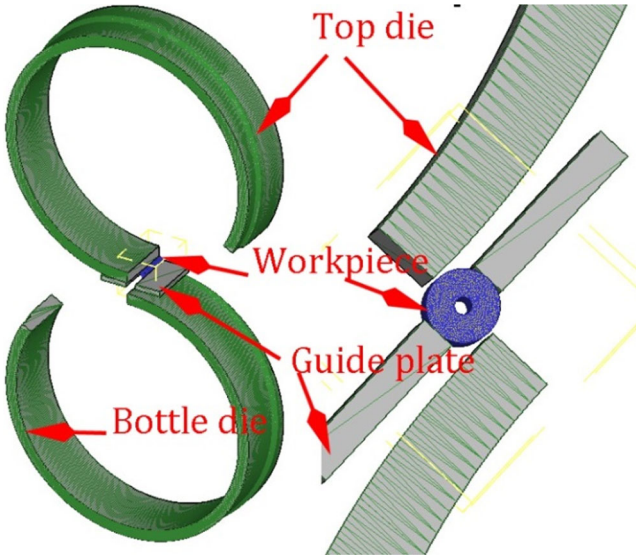

Fig. 1 Geometry mode of CWR for DEFORM-3D

of CWR plate pieces is flattened. Pater et al. [17–20] presented numerical and experimental findings regarding the production of hollow parts using a new method of rotary compression. The researchers analyzed wall thickness on the basis of the rotary compression process for hollow parts. Winiarski et al. [21] employed a new process for the formation of triangular flange in hollow shafts from Ti6Al4V alloy. Peng et al. [22] studied the stress distributions during the CWR of composite 42CrMo/Q235 laminated shafts. Zhang et al. [23] analyzed the effect of technological parameter on the microstructure of GH4169 alloy during the CWR process. Ying et al. [24] analyzed the temperature distribution in the CWR process. Sun et al. [25] studied the microstructure characteristics in high-carbon steel rod after warm CWR. Pater et al. [26] studied three-roll CWR without a mandrel for forming hollow shafts. The researchers analyzed the parameters of the CWR process by numerical simulation.

Table 1 Parameter of CWR simulation

Parameter	Value
Speed of roll (rpm)	10
Initial temperature of workpiece (°C)	1150
Die temperature (°C)	20
Environment temperature (°C)	20
Heat transfer coefficient (N s^{-1} mm^{-1} $°C^{-1}$)	40
Convection coefficient (N s^{-1} mm^{-1} $°C^{-1}$)	0.02
Friction factor(workpiece and die)	0.9
Friction factor(workpiece and guide)	0.1
Mesh number for billet	60,000
Mold material	4Cr5MoSiV1
Billet material	4Cr9Si2

Table 2 main process parameters for simulation

Item	Forming angle α (°)	Stretching angle β (°)	Area reduction Ψ (%)
1	30, 35, 38, 40	5–4	65.9
2	35	3.5, 4.5–4, 5, 5–4, 6, 6.5–6	65.9
3	35	5–4	59.5, 65.9, 51

Moreover, the plate wedge rolling processes of hollow shafts were examined comparatively.

Material property is an important factor in the performance of hollow valves [5]. Quan et al. [27] studied 3Cr20Ni10W2 heat-resistant alloy constitutive modeling for the dynamic recrystallization kinetics of as-extruded steel on the basis of stress–strain data. Shi et al. [28] analyzed the characterization of the hot deformation behavior of GH925 superalloy by using constitutive equation, processing map, and microstructure observation. Lin et al. [29–34] proposed new phenomenological constitutive models to describe the thermo-viscoplastic response of Al–Zn–Mg–Cu and Al–Cu–Mg alloys under hot working conditions. In their proposed models, the material constants are presented as functions of strain rate, forming temperature, and strain. Furthermore, a modified Johnson–Cook model were established to predict the hot deformation behavior of 20CrMo alloy steel, 42CrMo steel, B steel sheet, and Ti matrix composites.

4Cr9Si2 steel is a representative valve steel. Given its good balance of strength, toughness, and wear resistance, 4Cr9Si2 is mainly used in the manufacture of boilers, steam turbines, power machinery, industrial furnaces, and aviation equipment and in petrochemical and industrial processes under high temperatures. To obtain practical process parameters, the material characteristic of 4Cr9Si2 steel during the hot forming process was studied in depth [35–39].

In this paper, a CWR process of hollow valves with 4Cr9Si2 steel is proposed. The objective is to investigate the material characteristic of 4Cr9Si2 steel during the hot forming process by isothermal compression tests and then establish the

Table 3 The main chemical composition of 4Cr9Si2 steel (mass fraction, %)

Element	Wt.%
C	0.35~0.50
Si	2.00~3.00
Mn	≤0.70
Cr	8.00~10.00
Ni	≤0.60
P	≤0.035
S	≤0.030

Table 4 The strain value of the node

NO	Radial strain	Tangential strain	Axial strain
P3	0.300	−0.412	0.877
P4	0.099	−0.469	1.185
P5	−0.009	−0.355	1.134
P6	−0.424	0.076	1.116
P7	−0.592	0.250	1.113
P8	−0.632	0.317	0.995
P9	−0.512	0.281	0.872

optimum process parameters of the CWR process of hollow valves with 4Cr9Si2 steel. Furthermore, the influence of the process parameters of the internal hole diameter was analyzed. The proposed changes decrease the stretching angle of inner hole reaming.

2 Finite element models and process parameters

On the basis of DEFORM-3D software, the simplified finite element models of CWR for preform hollow valves were established. The geometry model shown in Fig. 1 consists of a workpiece, two rolls, and two guide plates. To establish the FE model of CWR, the following assumptions were made [5]:

1. The tools and guide plates were rigid. Given the negligible elastic deformation of tools and guide plates, two wedged tools and guide plates were considered rigid models for the tool materials.
2. A billet was a plastic material model. During formation, a billet was characterized by significant plastic deformation. The extent of elastic deformation was slight; thus, it can be disregarded.
3. A roll rotates at a fixed step. In practical rolling, roll speed first increases rapidly, stabilizes to a constant rate, and then decelerates.
4. Only half of the model was simulated to maintain asymmetrical CWR and to reduce CPU processing time.
5. The friction coefficient was assumed constant throughout the CWR process regardless of whether or not cooling water was used. The frictional force in the shear friction model was defined by the following:

$$f_s = m \times k \tag{1}$$

where $\mathbf{f_s}$ is the frictional stress, **k** is the shear yield stress, and **m** is the friction factor.

Table 1 summarizes the adopted simulation parameters of the CWR process. The main process parameters for simulation are listed in Table 2.

3 Material characteristic of 4Cr9Si2 steel during the cross wedge rolling process

3.1 Experimental hot forming procedures

The chemical composition of 4Cr9Si2 in this study is given in Table 3. Cylindrical compression specimens of 8 mm in diameter and 15 mm in height were made. Hot uniaxial compression tests were conducted to characterize the flow behavior of 4Cr9Si2 on a Gleeble 1500 thermo-mechanical simulator at the University of Science and Technology Beijing in Beijing. Graphite foils were used to prevent specimens from sticking on the anvil at high temperatures and to enhance electric resistance. K-type thermocouples welded in the center of the specimens were employed to measure and control the temperature. Figure 2a shows the specimens before compression. Each sample was heated to deformation temperature at a rate of 10 °C s^{-1} by thermo-coupled feedback-controlled AC current, and held for 5 min at isothermal conditions before compression tests, in order to obtain the heat balance. Compression were conducted isothermally at the

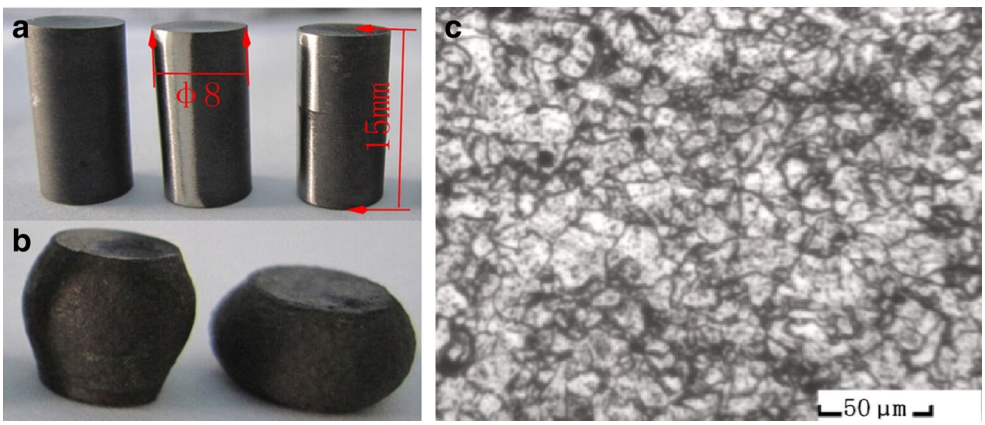

Fig. 2 Specimens and microstructure of 4Cr9Si2 steel: **a** before compression and **b** after compression; **c** microstructure of martensite

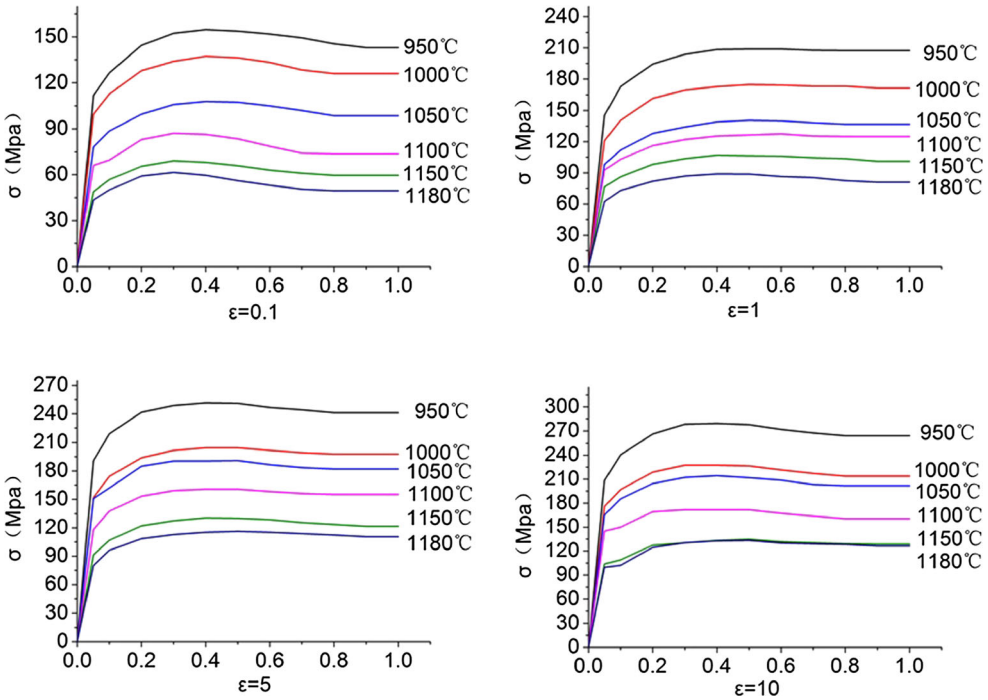

Fig. 3 Flow stress–true strain curves for 4Cr9Si2 steel under different forming temperatures with strain rates of **a** 0.1 s^{-1}, **b** 1 s^{-1}, **c** 5 s^{-1}, and **d** 10 s^{-1}

temperature ranging from 950 to 1180 °C and the strain rates ranging from 0.1 to 10 s^{-1}. After hot compression, the specimens were immediately quenched by water to retain the microstructures. Figure 2b shows the specimens after compression, and Fig. 2c shows the microstructure after compression. The microstructural characteristic and physical properties of 4Cr9Si2 steel after isothermal compression tests were investigated.

3.2 Determination of material constants

By using the load–displacement data recorded by the thermo-simulation machine, the flow stress–true strain curves of 4Cr9Si2 steel were obtained at various temperatures and strain rates (Fig. 3). A lower forming temperature, as well as a higher strain rate, corresponds to higher flow stress. During the early stage of the hot forming process, the flow stresses increase sharply because work hardening. After reaching the peak flow stresses, the curves exhibit remarkable steady or even a descendent stage as a result of the equilibrium of work hardening and dynamic softening. Generally, the flow stress and strain rate decrease with increasing forming temperature because a higher forming temperature and lower strain rate provide longer energy accumulation and higher boundary mobility. This phenomenon leads to dislocation annihilation and rearrangement, which decrease the flow stress level [40, 41].

Constitutive equations are usually used to estimate the flow behavior of a material during the plastic deformation process. The correlation between flow stress, forming temperature, and strain rate, particularly at high forming temperatures, can be widely expressed by the Arrhenius-type equation. Furthermore, the effects of the forming temperature and strain rate on the flow behavior of a material can be expressed by the Zener–Hollomon parameter **Z** in an exponent-type equation [42–48].

Those equations were expressed as Eqs. (2) and (3). Subsequently, these constitutive equations were adopted to estimate the plastic flow behavior of 4Cr9Si2 steel under the hot forming condition. The flow stress–true strain relationship obtained from the compression tests would be used to determine the material constants in these constitutive equations.

$$Z = \varepsilon \exp\left(\frac{Q}{RT}\right) \tag{2}$$

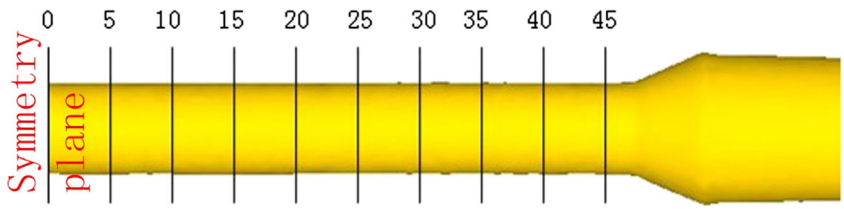

Fig. 4 Workpiece cross section position

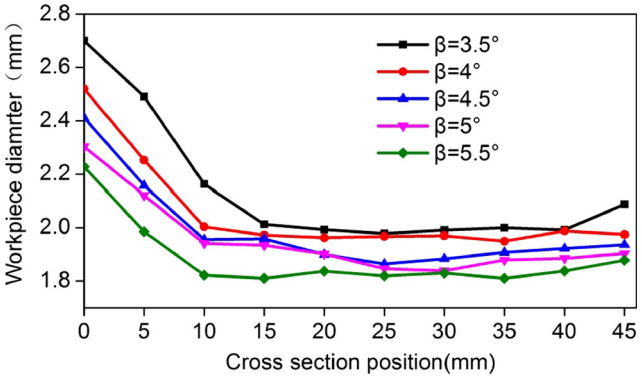

Fig. 5 Comparison of inner diameter values of different stretching angles

$$\varepsilon = AF(\sigma)\exp\left(-\frac{Q}{RT}\right) \tag{3}$$

$$F(\sigma) = \begin{cases} \sigma^{n'} \\ \exp(\beta\sigma) \\ [\sinh(\alpha\sigma)]^{n} \end{cases} \tag{4}$$

where σ is the flow stress (MPa) for a given strain, $\dot{\varepsilon}$ is the strain rate (s^{-1}), T is the absolute temperature (K), R is the universal gas constant (8.3145 J mol^{-1} K^{-1}), Q is the activation energy of deformation (J mol^{-1}), and A, n_0, n, b, and $a(a = b/n_0)$ are the material constants.

The material constants in the above constitutive equations were evaluated at the peak stress. After a series of mathematical calculations, the developed constitutive equation for 4Cr9Si2 steel during the hot compress process could be expressed as follows:

$$\varepsilon = e^{34.589}[\sinh(0.00907\sigma)]^{5.0942}\exp\left(-400119\Big/RT\right) \tag{5}$$

The Zener–Hollomon parameter for 4Cr9Si2 steel could be represented as follows:

$$Z = \varepsilon\exp\left[400119\Big/(RT)\right] = e^{34.589}[\sinh(0.00907\sigma)]^{5.0942} \tag{6}$$

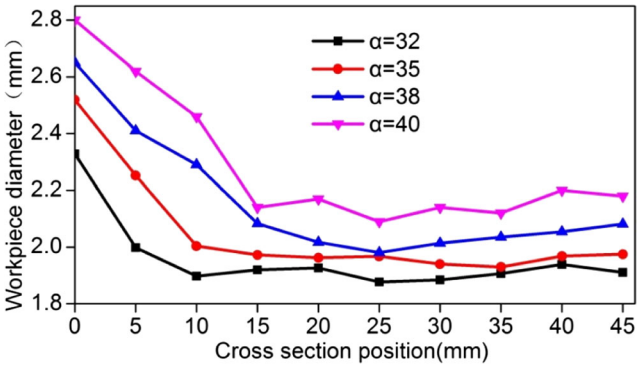

Fig. 7 Comparison of the inner diameter of different forming angles

The constitutive equation for 4Cr9Si2 steel during the CWR process could be expressed by the Zener–Hollomon parameter:

$$\sigma = \frac{1}{0.00907}\ln\left\{\left(\frac{Z}{e^{34.589}}\right)^{1/5.0942} + \left[\left(\frac{Z}{e^{34.589}}\right)^{2/5.0942} + 1\right]^{1/2}\right\} \tag{7}$$

The strain could seriously influence the flow stress during the compression tests. In the following section, the plastic flow behavior of 4Cr9Si2 steel during the hot compress process was imported to DEFORM-3D software to study the CWR for preform hollow valves.

4 Cross wedge rolling process for preform hollow valves with 4Cr9Si2 steel

4.1 Effects of stretching angle on inner diameter

The inner diameter was analyzed by changing a single factor [49]. The diameter of the billet was set to φ12 × 6 mm. The compression ratio was 0.42, and the initial temperature of the workpiece was 1150 °C. Figure 4 shows the half of the workpiece that has zero plane of symmetry every 5 mm from a cross section. According to the aforementioned method, each section of the strip was obtained. Figure 5 shows the

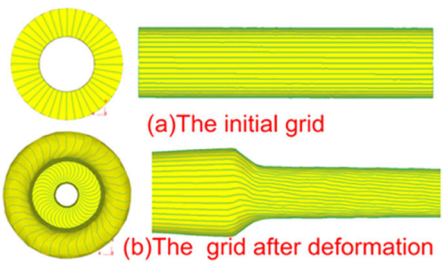

a The deformation grid during the CWR process

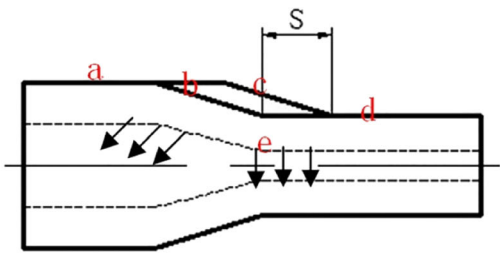

b Theoretical analysiss of metal flow

Fig. 6 Metal flow. **a** The deformation grid during the CWR process. **b** Theoretical analysis of metal flow

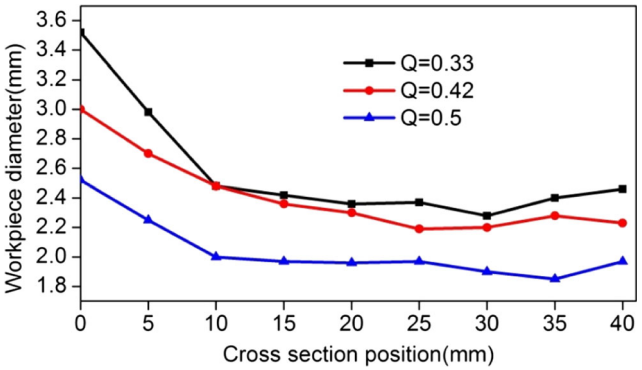

Fig. 8 Influence of the relative wall thickness to diameter change ($\alpha = 35°$, $\beta = 4°$)

workpiece diameter values under a forming angle of 35°, relative wall thickness of 0.5, and different stretching angles.

Under different stretching angles, the change trend of workpiece diameter size is basically the same. Given the hole shrinkage, wall thickness reduction, and stretching angle increase, the thickness reduction thin rate gradually decreases with the gradual decrease in inner diameter. General wedging position inner ones, stretching the end period of inner diameter is big.

At the same stretching angle, different rolling positions have fluctuant behavior and show a declining tendency within the range of 0–15 mm. Within the length of 15–45 mm, the rolling positions exhibit small fluctuations. The wedging position in the rolled piece hole and shrinkage pore volume is smaller than the other parts of the rod part shrinkage hole.

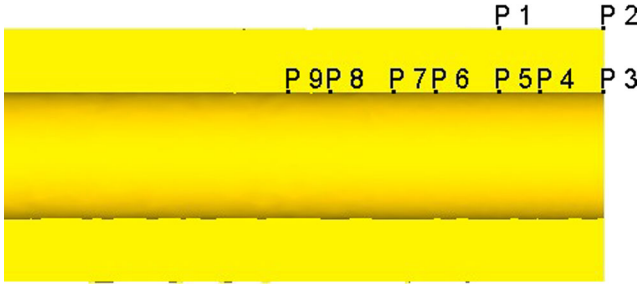

Fig. 10 Rolled piece node location map

Rolling occurs in the hole reaming phenomenon at 0–15 mm. The inner hole of the fluctuations without mandrel reflects the uncontrollable metal deformation characteristics of the tube surface.

The instantaneous rolling-stretching $\boldsymbol{S}$ could be represented as follows:

$$S = \frac{1}{2}\pi d_k \tan\beta \tag{8}$$

The radial compression quantity $\boldsymbol{Z_0}$ could be represented as follows:

$$Z_0 = \frac{1}{2}\pi d_k \tan\beta \tan\alpha \tag{9}$$

where $\boldsymbol{d_k}$ is the diameter of rolled piece, β is the stretching angle, and α is the forming angle.

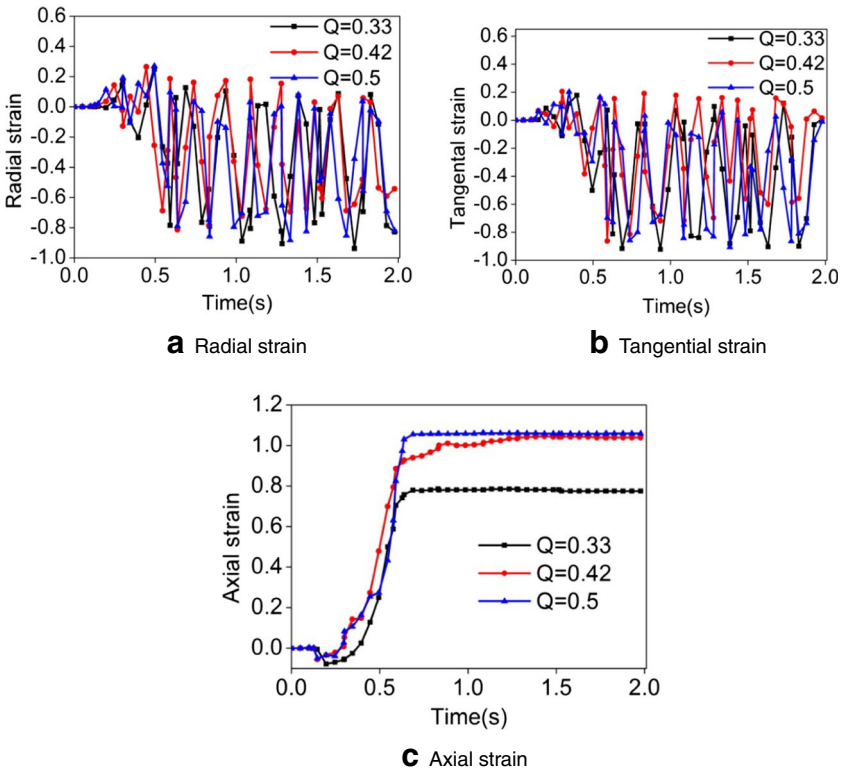

Fig. 9 The inner surface under different relative wall thickness strain change. **a** Radial strain. **b** Tangential strain. **c** Axial strain

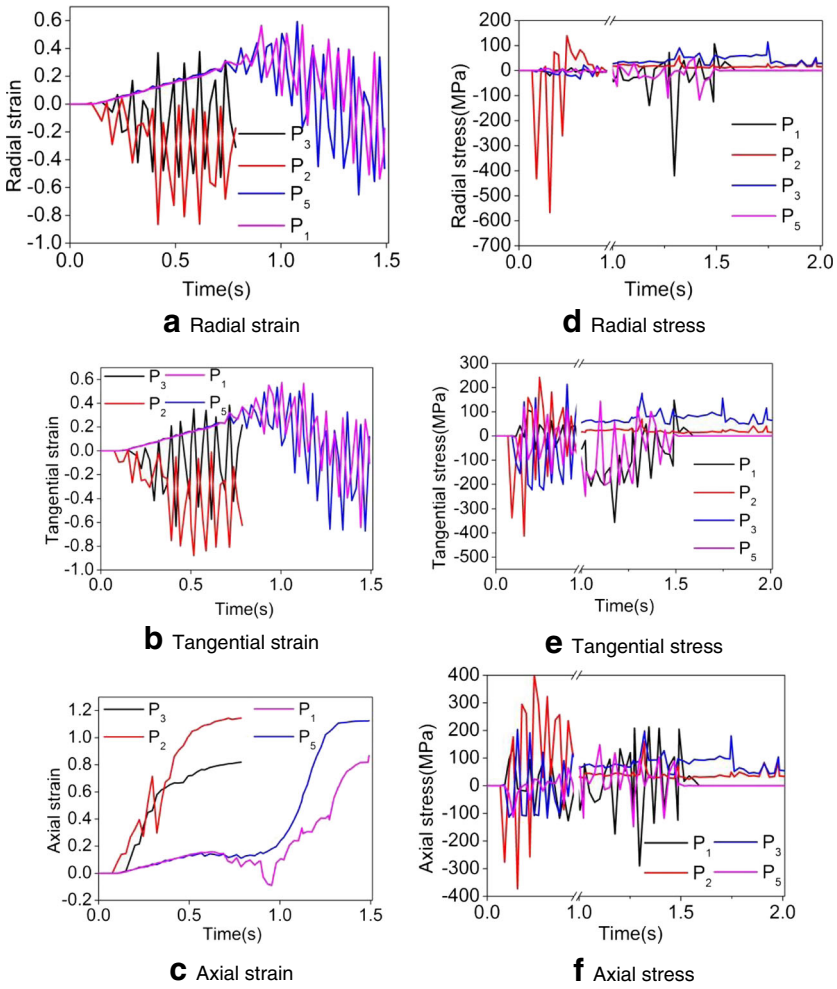

Fig. 11 Node stress–strain diagram ($\alpha = 35°$, $\beta = 3.5°$, $\Psi = 65.9\ \%$, $T = 1150\ °C$). **a** Radial strain. **b** Tangential strain. **c** Axial strain. **d** Radial stress. **e** Tangential stress. **f** Axial stress

As can be seen from Eqs. (8) and (9), when the forming angle is constant, the stretching angle increases, and the maximum amount of the instantaneous rolling-stretching $\boldsymbol{S}$ radial compression of $\mathbf{Z_0}$ increases. Figure 6a shows the initial grid and the grid after deformation. Figure 6b shows the metal flow. The metal in the ***cde*** region is radially compressed, whereas that in the ***abcd*** region is mainly radial compression and axial extension. With increasing stretching angle, the deformation zone transient stretching increases. The ***cde*** area also increases because of the buildup of friction and metal axial flow difficulties along the radial flow of the metal. The wall thickness increases with the increase in stretching angle and decrease in workpiece diameter.

4.2 Effects of forming angle on inner diameter

Figure 7 shows the different forming angles, the change trend of rolling diameter size, and the internal hole shrinkage with decreasing wall thickness. An increase in the bending angle leads to a gradual increase in diameter values. At the same forming angle and different stretching angle conditions, the different workpiece diameters have similar fluctuations. The rolling up position appears on both sides of the wedge hole reaming phenomenon and decreased in the range of 0–15 mm. The 15–45 mm position fluctuated slightly from the maximum wedge position of the workpiece diameter.

4.3 Effects of billet relative wall thickness to diameter change

Figure 8 shows the diameter variation of different relative thickness under the forming angle 35° and stretching angle 4°. The workpiece size was φ12 × 6 mm, φ12 × 7 mm, and φ12 × 8 mm. Figure 8 shows that the workpiece diameter increases with decreasing relative wall thickness. When the relative wall thickness is 0.33, the workpiece thickness relative to the original thickness will increase. To obtain the different relative wall thicknesses of the workpiece, the workpiece diameter change rate was calculated. When the relative wall thickness is 0.33, 0.42, and 0.5, the value is 70.2, 67.7, and 66 %, respectively. This result shows a decreasing trend of relative wall thickness.

Figure 9 is the strain changes of the rolled piece at the internal surface. Radial strain and tangential strain have slight

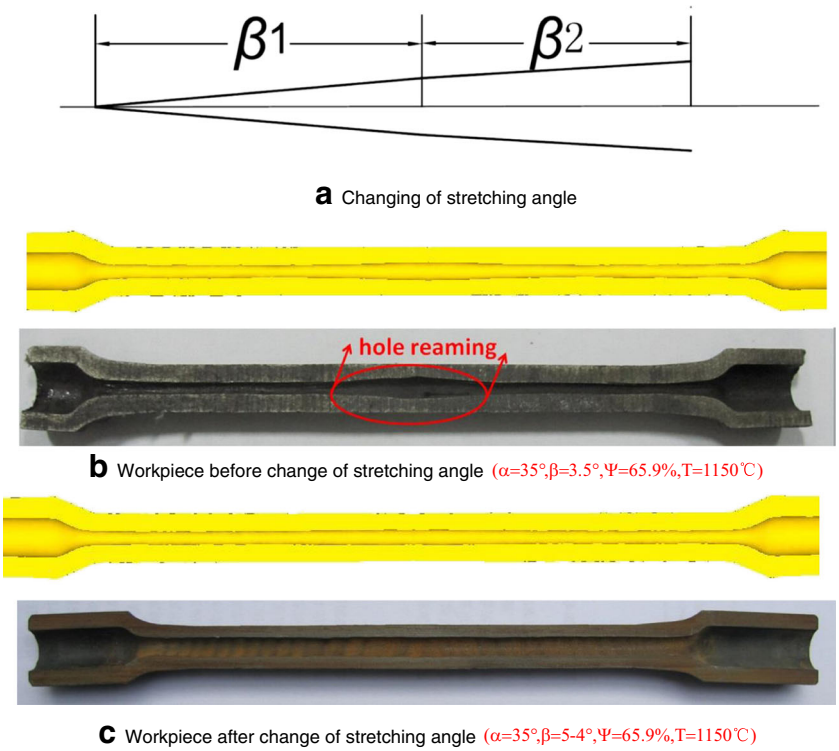

Fig. 12 Comparison of stretching angle before and after the change. **a** Changing of stretching angle. **b** Workpiece before change of stretching angle ($\alpha = 35°$, $\beta = 3.5°$, $\Psi = 65.9\ \%$, $T = 1150\ °C$). **c** Workpiece after change of stretching angle ($\alpha = 35°$, $\beta = 5–4°$, $\Psi = 65.9\ \%$, $T = 1150\ °C$)

differences under different relative wall thicknesses. Axial strain increases with increasing relative wall thickness. When the relative wall thickness is 0.33, the axial strain value is approximately 0.78. When the relative wall thickness is 0.5, axial strain value is 1.06. With increasing relative wall thickness, the rolling resistance deformation ability increases and the inner deformation becomes difficult to roll. Metal was forced by the axial flow to the inner surface of the metal formation tensile force. Therefore, the variation of the diameter decreases with thinning wall thickness.

5 Rolled piece up wedge position on both sides of the inner hole reaming

An uneven inner hole leads to the uneven thickness of rolled pieces. This factor will affect the product after processing. By using a forming angle of 35°, stretching angle of 3.5°, workpiece diameter of 12 mm, relative wall thickness of 0.5, and compression ratio rolled pieces at 0.42, hole symmetry reaming and its solution were studied. Figure 10 shows the symmetry center of rolled pieces node P2, distance of P3 from the center of the symmetry plane to the 5 mm cross section of P1, and distances of P5 from the center of the symmetry plane at 3, 8, 10, 13, and 15 mm of inner surface nodes P4, P6, P7, P8, and P9, respectively.

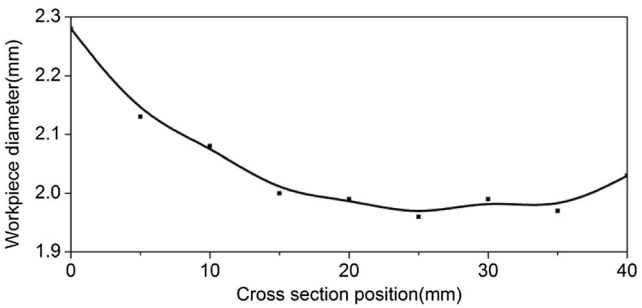

Fig. 13 Change of stretching angle workpiece diameter values ($\alpha = 35°$, $\beta = 5–4°$, $\Psi = 65.9\ \%$, $T = 1150\ °C$)

Figure 11 shows the comparison of the stress and strain of P1, P2, P3, and P5. The strain value of each section is shown in the figure. In the symmetry plane of the wedge section, the deformation of surface node P3 falls behind the external surface of P2. In the early stages of deformation, deformation moves gradually to the inner layer metal. When the pressure reaches a certain value, the inner surface of the metal begins to deform. The radial compression of the inner surface points is not conducive to inner hole shrinkage, thus showing that the radial pressure strain at P2 before P3 and at the 0.17 s point is pulled by the outer metal.

In die wedge rolling, the surface of the metal mold will exhibit slanting wedge compression axial flow. The inner surface of the metal is hardly affected by force; thus, the 0.1 s point of P2 has evident axial strain and the P3 axial strain is zero.

In the wedging zone, the small contact area of the workpiece and die leads to low metal axial flow capacity and a slow trend of flowing enhancement. The center of symmetry planes P2 and P3 experiences compressive strain after several weeks,

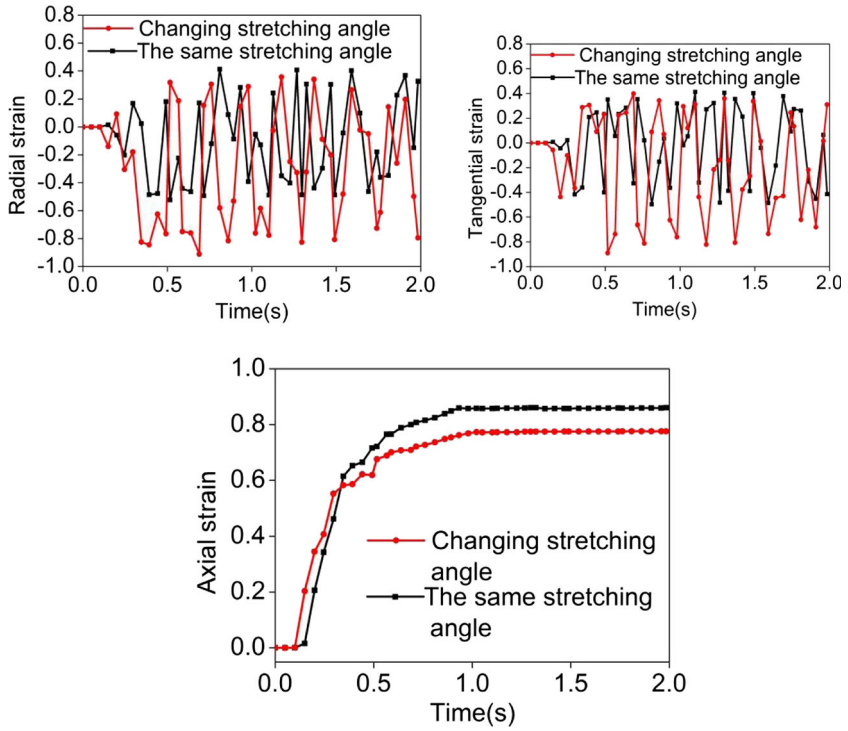

Fig. 14 Strain comparison of variable stretching angle

and strain P2 has a greater value than P3. The 0–0.4 s moments of deformation to the initial wedge section and symmetrical center surface of the inner surface of the anisotropic strain point are delayed, and the strain value is less than the appearance of pastry. The deformation of broadening region is enhanced, the difference between inner and outer surface is reduced, and the strain difference of P5 and P1 in the broadening region (0.9–1.3 s) is small. The axial strain of P5 is higher than P1.

The stress value of the inner surface of the main deformation area is less than that of the outer surface. The stress value of P2 and P1 is 0, and the stress value of P5 and P3 in the center symmetry is 3. The stress state of P3 is obvious, and the radial tensile stress is not conducive to the radial flow.

Table 5 Variable stretching angle after forming the rolling node strain value

NO	Radial strain	Tangential strain	Axial strain
P3	−0.105	−0.390	0.786
P4	−0.283	−0.359	1.043
P5	−0.488	−0.154	1.016
P6	−0.660	0.029	1.055
P7	−0.728	0.152	1.017
P8	−0.821	0.141	0.962
P9	−0.691	0.073	0.917

The whole rolling precision surface nodes in anisotropic strain values are shown in Table 2. With increasing distance from the workpiece center of the symmetry plane, the radial strain of the metal has a significant tensile strain transition into compressive strain and exhibits an increase in strain value. The tangential strain in the pressure transition strain is a tensile strain, and the strain value decreases. In the center of symmetry, the radial strain of the P3 point is the tensile strain and the tensile stress state is the same as that in Fig. 12d. The tangential strain value is larger than that of the normal stretching section, and the axial strain value is small, which is not favorable to the deformation of inner hole. After the completion of the phase transition of rolling radial strain in point P5, where the section is located in the center of symmetry, the basic and inner hole reaming end position is at 16 mm. In P8 and P9, the endpoint is located in the outer end because of the influence of axial strain.

In summary, the rolling up position on both sides of wedge hole reaming is mainly due to the small wedge initial tooling of the rolling impact area. The deformation does not completely penetrate the normal stretching segment. Compared with the obvious differences in the inner layer and outer layer of the metal flow, the inner layer metal deformation lags behind the metal outer layer and prevents hole shrinking deformation in the surface metal during radial tensile strain. With increasing distance from the wedge position, the penetration ability of workpiece deformation is improved. The inner hole reaming trend gradually decreases with the gradual increase in the inner surface of metals during radial compressive strain.

a H500 mill **b** Electric Tube Furnace

Fig. 15 Experimental equipment. **a** H500 mill. **b** Electric tube furnace

The hollow valve without mandrel in the CWR hole and shrinkage hole influence the research and analysis of wedge position on both sides of the hole reaming. This study proposes a stretching angle design to improve the workpiece reaming location of the metal flow state of the CWR die and improve the rolling inner hole reaming phenomenon. The design of the changing angle wedge is stretched to remove the need for reaming stretching angle in the mold, as shown in Fig. 12a.

Figure 12b, c shows the comparison of the stretching angle before and after the change. When the forming angle is 35°, the wedge stretches to 30 mm at a stretching angle of 5° and the other position stretching angle is 4°. The results show that the proposed method significantly improves the wedge position hole reaming phenomenon.

Figure 13 shows the stretching angle workpiece with different cross section positions of the diameter variable. The wedge position diameter value is 2.28, and the distance symmetry plane at 15 to 40 mm has a position diameter value of 2 mm and rolls along the axial error under control.

Figure 14 shows the change before and after the rolling up of the stretching angle comparison of the wedge position within the surface point strain. With changing stretch angle, the wedge position stretches to 30 mm and the stretching angle increases. Furthermore, the wedging zone node strain changes significantly. At 0.15 s, the node radial strain is 0.015 at a 0.14 compressive strain, the tensile strain is 0.009 for a 0.057 compressive strain. The axial tensile strain increases from 0.015 to 0.203. In the deformation process, the radial pressure strain of the joint obviously increases and the strain of the die decreases.

Figure 10 shows the node position of forming the P3–P9 strain value. Table 5 shows the radial compressive strain of the rolled piece surface. The difference between the axial strain value of P4 and P5 in wedge position 0.257 and 0.23 is 0.308 and 0.257, respectively (Table 4). The radial compression of the metal in the inner part of the wedge increases, the tangential flow trend decreases, and the axial extension is improved.

The strain value comparison shows that changing the stretching angle significantly changes the metal flow of the surface and reduces the reaming position metal strain value gap. This process achieves uniformity in pore size.

Table 6 The main technical parameters of H500

Parameter	Value
Roll speed (r min^{-1})	10/12/15
Motor power (kW)	36
Roll diameter (mm)	500
Roll width (mm)	450
The maximum diameter of the rolling (mm)	40
The maximum length of rolling (mm)	400

6 Experimental tests

The experimental tests on the CWR process were conducted by using the H500 mill and electric tube furnace at the University of Science and Technology Beijing, China. The H500 mill and the electric tube furnace are shown in Fig. 15a, b, respectively. The main technical parameters are listed in Table 6, and the main technical characteristics are

Table 7 The main technical parameters of electric tube furnace

Parameter	Value
Power rating (kW)	4
Rated temperature (°C)	1200
Rated voltage (V)	220
Chamber size (mm)	Φ60 × 1000

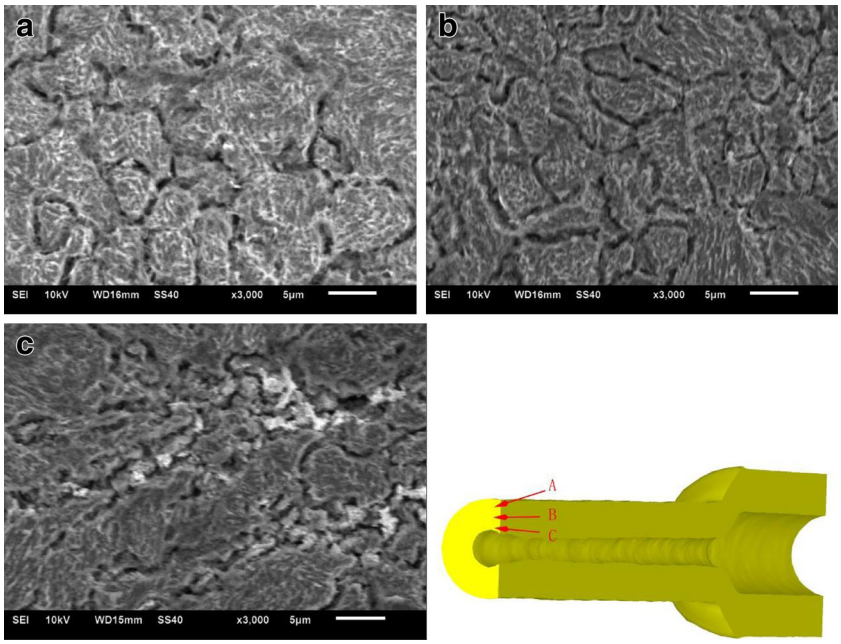

Fig. 16 Microstructure of CWRed hollow valve ($\alpha = 35°$, $\beta = 5–4°$, $\Psi = 65.9\ \%$, $T = 1150\ °C$)

listed in Table 7. The experimental billets were provided by an autoparts company.

Figure 16 shows the microstructure of the CWRed hollow valve. During the CWR process, dynamic recrystallization occurs. The 4Cr9Si2 steel rolling grains are isometric after rolling. The grains do not show obvious elongation, and all rolled grains undergo dynamic recrystallization to meet the grain size requirements of the valves.

Figure 17 shows the diameter of CWR hollow valve by experiment and simulation. The original diameter is φ12 × 6 mm. After rolling, the outer diameter is 7.0 mm. The experiment and simulation of CWR show good agreement.

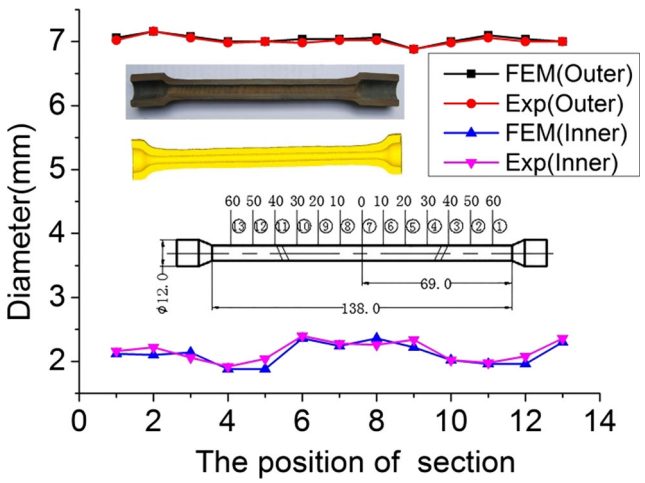

Fig. 17 The diameter of CWR hollow valve by experiment and simulation ($\alpha = 35°$, $\beta = 5–4°$, $\Psi = 65.9\ \%$, $T = 1150\ °C$)

7 Conclusions

The following conclusions are drawn:

1. The relationship among peak stress, deformation temperature, and strain rate can be described as follows:

$$\varepsilon = e^{34.589}[\sinh(0.00907\sigma)]^{5.0942} \exp\left(-400119 \Big/ RT\right)$$

2. The increase in stretching angle, difficulties in rolled metal axial flow, and accumulation of metal increase the workpiece thickness and decrease the workpiece diameter. The forming angle increases, axial metal flow capacity increases, the inner layer metal radial compression degree decreases, and workpiece diameter increases. Furthermore, the blank relative wall thickness increases, the piece in metal layer by the radial pressure decreases, the amount of axial metal flow increases, and the workpiece diameter decreases.
3. The workpiece position on both sides of the wedge hole reaming is mainly due to the small wedge initial tooling of rolling impact zone. Furthermore, the deformation does not fully penetrate the workpiece. The inner layer metal deformation lags behind the metal outer layer. The inner hole shrinking decreases in the metal surface under radial tensile strain.
4. The variable stretching angle design of the mold can significantly improve the wedge position on both sides of the inner hole reaming phenomenon. This approach increases the reaming position stretching angle, and adding an angle of 1° is appropriate.

Acknowledgments The authors thank the guidance from Professor Jianguo Lin at Imperical College London. This work is supported by the National Natural Science Foundation of China (Grant No. 51375042). This work is also supported by YangFan Innovative and Entepreneurial Research Team Project (No. 201312G02). This project is also supported by China Postdoctoral Science Foundation (Grant No. 2015M580977).

Compliance with ethical standards

Conflict of interest The authors declare no conflict of interest.

References

1. El Mehtedi M, Ricci P, Drudi L, El Mohtadi S, Cabibbo M, Spigarelli S (2012) Analysis of the effect of deep cryogenic treatment on the hardness and microstructure of X30CrMoN151 steel. Mater Des 33:136–144. doi:10.1016/j.matdes.2011.07.030
2. Zhu Y, Zhimin Y, Jiangpin X (2011) Microstructural mapping in closed die forging process of superalloy Nimonic 80a valve head. J Alloys Compd 509:6106–6112. doi:10.1016/j.jallcom.2011.03.038
3. Jeong HS, Cho JR, Park HC (2005) Microstructure prediction of Nimonic 80A for large exhaust valve during hot closed die forging. J Mater Process Technol 162–163:504–511. doi:10.1016/j.jmatprotec.2005.02.101
4. Jeong HS, Cho JR, Lee NK, Park HC (2006) Simulation of electric upsetting and forging process for large marine diesel engine exhaust valves. Mater Sci Forum 510–511:142–145. doi:10.4028/www.scientific.net/MSF.510-511.142
5. Ji H, Liu J, Wang B, Zheng Z, Huang J, Hu Z (2015) Cross-wedge rolling of a 4Cr9Si2 hollow valve: explorative experiment and finite element simulation. Int J Adv Manuf Technol 77:15–26. doi:10.1007/s00170-014-6363-9
6. Hu Z, Zhang K, Wang B, Shu X (2004) Formed technology and simulation of parts about the cross-wedge rolling, vol 1–10. The Publishing House of Metallurgical Industry, Beijing, pp 180–185
7. Zhou J, Xiao C, Yu Y, Jia Z (2013) Influence of tool parameters on tool wear in two-roll cross-wedge rolling. Int J Adv Manuf Technol 65:745–753. doi:10.1007/s00170-012-4213-1
8. Kache H, Stonis M, Behrens BA (2012) Development of a warm cross wedge rolling process using FEA and downsized experimental trials. Prod Eng 6:339–348. doi:10.1007/s11740-012-0379-5
9. Xiong Y, Sun S, Li Y, Zhao J, Lv Z, Zhao D, Zheng Y et al (2006) Effect of warm cross-wedge rolling on microstructure and mechanical property of high carbon steel rods. Mater Sci Eng A 431:152–157. doi:10.1016/j.msea.2006.05.148
10. Pater Z, Gontarz A, Weroński W (2006) Cross-wedge rolling by means of one flat wedge and two shaped rolls. J Mater Process Technol 177:550–554. doi:10.1016/j.jmatprotec.2006.03.232
11. Pater Z (2000) Theoretical and experimental analysis of cross wedge rolling process. Int J Mach Tools Manuf 40:49–63. doi:10.1016/S0890-6955(99)00047-4
12. Dong Y, Tagavi KA, Lovell MR (2000) Analysis of interfacial slip in cross-wedge rolling: a numerical and phenomenological investigation. J Mater Process Technol 97:44–53. doi:10.1016/S0924-0136(99)00285-X
13. Deng Z, Lovell MR, Tagavi KA (2001) Influence of material properties and forming velocity on the interfacial slip characteristics of cross wedge rolling. J Manuf Sci Eng 123:647. doi:10.1115/1.1383028
14. Wang MT, Li XT, Du FS (2009) Analysis of metal forming in two-roll cross wedge rolling process using finite element method. J Iron Steel Res Int 16:38–43
15. Urankar S, Lovell M, Morrow C, Li Q, Kawada K (2006) Development of a critical friction model for cross wedge rolling hollow shafts. J Mater Process Technol 177:539–544. doi:10.1016/j.jmatprotec.2006.04.048
16. Urankar S, Lovell M, Morrow C, Li Q, Kawada K (2006) Establishment of failure conditions for the cross-wedge rolling of hollow shafts. J Mater Process Technol 177:545–549. doi:10.1016/j.jmatprotec.2006.04.052
17. Tomczak J, Pater Z, Bulzak T (2015) The influence of hollow billet thickness in rotary compression. Int J Adv Manuf Technol. doi:10.1007/s00170-015-7437-z
18. Tomczak J, Bulzak T, Pater Z, Abspoel M (2015) The effect of billet wall thickness on the rotary compression process for hollow parts. Strojniški vestnik J Mech Eng 61:149–156. doi:10.5545/sv-jme.2014.1977
19. Tomczak J, Pater Z, Bulzak T (2015) Forming of hollow shaft forging from titanium alloy Ti6Al4V by means of rotary compression. Arch Metall Mater 60:419–425. doi:10.1515/amm-2015-0069
20. Pater Z, Gontarz A, Tomczak J, Bulzak T (2015) Producing hollow drive shafts by rotary compression. Arch Civ Mech Eng. doi:10.1016/j.acme.2014.10.002
21. Winiarski G, Gontarz A, Pater Z (2015) A new process for the forming of a triangular flange in hollow shafts from Ti6Al4V alloy. Arch Civ Mech Eng. doi:10.1016/j.acme.2015.01.001
22. Peng WF, Zhang JH, Huang GX, Liu WP, Shu XD, Zhu J (2015) Stress distributions during the cross-wedge rolling of composite 42CrMo/Q235 laminated shafts. Int J Adv Manuf Technol. doi:10.1007/s00170-015-7541-0
23. Zhang N, Wang B, Lin J (2012) Effect of cross wedge rolling on the microstructure of GH4169 alloy. Int J Miner Metall Mater 19:836–842. doi:10.1007/s12613-012-0636-9
24. Ying FQ, Pan BS (2007) Analysis on temperature distribution in cross wedge rolling process with finite element method. J Mater Process Technol 187–188:392–396. doi:10.1016/j.jmatprotec.2006.11.193
25. Sun SH, Xiong Y, Zhao J, Lv ZQ, Li Y, Zhao DL, Fu WT (2005) Microstructure characteristics in high carbon steel rod after warm cross-wedge rolling. Scr Mater 53:137–140. doi:10.1016/j.scriptamat.2005.01.011
26. Bartnicki J, Pater Z (2004) The aspects of stability in cross-wedge rolling processes of hollowed shafts. J Mater Process Technol 155–156:1867–1873. doi:10.1016/j.jmatprotec.2004.04.278
27. Quan G, Mao A, Luo G, Liang J, Wu D, Zhou J (2013) Constitutive modeling for the dynamic recrystallization kinetics of as-extruded 3Cr20Ni10W2 heat-resistant alloy based on stress–strain data. Mater Des 52:98–107. doi:10.1016/j.matdes.2013.05.030
28. Shi Z, Yan X, Duan C (2015) Characterization of hot deformation behavior of GH925 superalloy using constitutive equation, processing map and microstructure observation. J Alloys Compd. doi:10.1016/j.jallcom.2015.08.118
29. Lin YC, Wen D, Deng J, Liu G, Chen J (2014) Constitutive models for high-temperature flow behaviors of a Ni-based superalloy. Mater Des 59:115–123. doi:10.1016/j.matdes.2014.02.041
30. Chen X, Lin YC, Wen D, Zhang J, He M (2014) Dynamic recrystallization behavior of a typical nickel-based superalloy during hot deformation. Mater Des 57:568–577. doi:10.1016/j.matdes.2013.12.072
31. Lin YC, Deng J, Jiang Y, Wen D, Liu G (2014) Hot tensile deformation behaviors and fracture characteristics of a typical Ni-based superalloy. Mater Des 55:949–957. doi:10.1016/j.matdes.2013.10.071
32. Lin YC, Chen M, Zhong J (2008) Effect of temperature and strain rate on the compressive deformation behavior of 42CrMo steel. J

Mater Process Technol 205:308–315. doi:10.1016/j.jmatprotec.2007.11.113

33. Lin YC, Chen X (2011) A critical review of experimental results and constitutive descriptions for metals and alloys in hot working. Mater Des 32:1733–1759. doi:10.1016/j.matdes.2010.11.048
34. Lin YC, Chen M, Zhong J (2008) Constitutive modeling for elevated temperature flow behavior of 42CrMo steel. Comput Mater Sci 42:470–477. doi:10.1016/j.commatsci.2007.08.011
35. Kim DJ, Kim DK, Kim DY, Ryu SH (2001) Application of nimonic 80A to the hot forging of an exhaust valve head. J Mater Process Technol 113:148–152. doi:10.1016/S0924-0136(01)00700-2
36. Park NK, Kim IS, Na YS, Yeom JT (2001) Hot forging of a nickel-base superalloy. J Mater Process Technol 111:98–102. doi:10.1016/S0924-0136(01)00489-7
37. Huo Y, Bai Q, Wang B, Lin J, Zhou J (2015) A new application of unified constitutive equations for cross wedge rolling of a high-speed railway axle steel. J Mater Process Technol. doi:10.1016/j.jmatprotec.2015.04.011
38. Li Y, Zhao S, Fan S, Yan G (2013) Study on the material characteristic and process parameters of the open-die warm extrusion process of spline shaft with 42CrMo steel. J Alloys Compd 571:12–20. doi:10.1016/j.jallcom.2013.03.209
39. Li H, Wei D, Li Y, Wang X (2012) Application of artificial neural network and constitutive equations to describe the hot compressive behavior of 28CrMnMoV steel. Mater Des 35:557–562. doi:10.1016/j.matdes.2011.08.049
40. Wang LX, Fang G, Leeflang MA, Duszczyk J, Zhou J (2015) Constitutive behavior and microstructure evolution of the as-extruded AE21 magnesium alloy during hot compression testing. J Alloys Compd 622:121–129. doi:10.1016/j.jallcom.2014.10.006
41. Chai R, Su W, Guo C, Zhang F (2012) Constitutive relationship and microstructure for 20CrMnTiH steel during warm deformation. Mater Sci Eng A 556:473–478. doi:10.1016/j.msea.2012.07.015
42. Xiao Y, Guo C (2011) Constitutive modelling for high temperature behavior of 1Cr12Ni3Mo2VNbN martensitic steel. Mater Sci Eng A 528:5081–5087. doi:10.1016/j.msea.2011.03.050
43. Tahami FV, Daei-Sorkhabi AH, Biglari FR (2010) Creep constitutive equations for cold-drawn 304L stainless steel. Mater Sci Eng A 527:4993–4999. doi:10.1016/j.msea.2010.04.055
44. Xiao J, Li DS, Li XQ, Deng TS (2012) Constitutive modeling and microstructure change of Ti-6Al-4V during the hot tensile deformation. J Alloys Compd 541:346–352. doi:10.1016/j.jallcom.2012.07.048
45. Fan XG, Yang H (2011) Internal-state-variable based self-consistent constitutive modeling for hot working of two-phase titanium alloys coupling microstructure evolution. Int J Plast 27:1833–1852. doi:10.1016/j.ijplas.2011.05.008
46. Yang L, Wang B, Liu G, Zhao H, Xiao W (2015) Behavior and modeling of flow softening and ductile damage evolution in hot forming of TA15 alloy sheets. Mater Des 85:135–148. doi:10.1016/j.matdes.2015.06.096
47. Zhou J, Wang B, Huang M (2014) Two constitutive descriptions of boron steel 22MnB5 at high temperature. Mater Des 63:738–748. doi:10.1016/j.matdes.2014.07.008
48. Yang X, Li W, Ma J, Hu S, He Y, Li L, Xiao B (2015) Thermo-physical simulation of the compression testing for constitutive modeling of GH4169 superalloy during linear friction welding. J Alloys Compd. doi:10.1016/j.jallcom.2015.09.267
49. Yang C, Hu Z (2015) Research on the ovality of hollow shafts in cross wedge rolling with mandrel. Int J Adv Manuf Technol. doi:10.1007/s00170-015-7478-3